JSER

Journal of Solar Energy Research (JSER)

Journal homepage: www.jser.ut.ac.ir

Numerical Design Optimization of a Scaled Solar Chimney Power Plant Using Guide-Assisted Collectors for Agricultural Applications- case study of Khenchela (Algeria)

Halima Boukhamla[a,b], Abdelmadjid Chehhat[a,b], Mohamed Si-Ameur[b]

[a]*Mechanical Engineering Department, Abbes Laghrour University of Khenchela Algeria*
[b]*LESEI (Laboratoire des Etudes des systèmes Energétiques Industriels) laboratory, University of Batna 2, Algeria*

ARTICLE INFO

Article Type:

Research Article

Received:2026.06.07
Accepted in revised form:2026.07.25

Keywords:
Solar chimney; Numerical simulation; Collector Convection; SCPP performances

A B S T R A C T

This research develops a theoretical framework for a solar chimney system comprising a collector, turbine, and vertical chimney. Global solar radiation and air temperature were calculated for midday on June 21st. The constructed model was utilized to simulate conditions using meteorological data from a specific summer day in Khenchela under realistic local climatic and operating conditions throughout summer while the physical proportions of Spain's Manzanares plant were reduced to one-tenth scale to project the facility's potential electricity yield. The effect of guides surrounding the collector on the electricity generated was simulated to determine the most effective SCPP for fulfilling the electricity demands of the agricultural area in Khenchela. The simulations revealed that an optimal configuration of nine guides could produce 72 W of electrical power. Results indicated that the efficiency of an SCPP is largely determined by its design dimensions, the surrounding air temperature, and the level of solar radiation.

1. Introduction

Solar Chimney Power Plants (SCPPs) represent a compelling renewable energy technology that harnesses solar radiation to generate electricity through a simple yet effective thermodynamic process. The system operates on the principle of a solar collector heating ambient air, which then rises through a tall central chimney due to buoyancy, driving one or more turbines to produce electrical power. While the technology gained fundamental validation from the pioneering 50 kW Manzanares

*Corresponding Author Email: boukhamla.halima@univ-khenchela.dz

Cite this article: Boukhamla, H., Chehhat, A. and Si-Ameur, M. (2026). Numerical Design Optimization of a Scaled Solar Chimney Power Plant Using Guide-Assisted Collectors for Agricultural Applications- case study of Khenchela (Algeria). Journal of Solar Energy Research, 11(3), 3152-3166. doi: 10.22059/jser.2026.410570.1756

DOI: 10.22059/jser.2026.410570.1756

©The Author(s). Publisher: University of Tehran Press.

prototype in Spain, its path to commercialization has been hindered by characteristically low conversion efficiency and significant capital costs[1-4]. These challenges had spurred a global research effort focused on geometric optimization, performance analysis, and system hybridization to enhance viability and power output[4, 5].

A substantial body of research has been dedicated to optimizing the geometry of SCPP components. For the collector, studies were moved beyond horizontal designs to investigate inclined configurations. For instance, Keshari et al. identified an optimal 6° inclination for the Manzanares plant, which significantly boosted theoretical power and airflow velocity[6]. These findings were supported by other CFD studies confirming that strategic roof inclinations positively alter convection patterns and increase mass flow rates[7, 8]. Furthermore, comprehensive parametric studies evaluating dozens of geometric configurations have revealed that even minor adjustments to parameters like chimney angle can lead to dramatic improvements in velocity and power output[9]. Simultaneously, chimney geometry was identified as a critical performance factor. Research demonstrated a paradigm shift from cylindrical to divergent or diffuser-type chimneys, which leverage pressure recovery effects to accelerate airflow and potentially triple power generation compared to conventional designs[10-12].

The power conversion unit, particularly the turbine, is another crucial focus area for optimization. Early research established mathematical models and CFD simulations for conventional axial turbines within SCPPs[2, 13]. However, a significant advancement had been the recent exploration of radial inflow turbines (RIF), which are better suited to the low-pressure, high-volume flow conditions in SCPPs. Studies dedicated to radial turbine design have shown they can achieve efficiency improvements of over 15% compared to axial configurations, offering a transformative potential for the technology[14, 15] .

The performance of these systems was not solely determined by their design but had also been highly sensitive to geographic and climatic conditions. Experimental and simulation studies across different regions, from the hot, arid climate of Algeria to various locations in Iran, had confirmed that local solar irradiance and ambient temperature cause substantial geographic variability in power output[16-19].

The research methodology for SCPPs had evolved significantly, with Computational Fluid Dynamics (CFD) emerging as the dominant tool for analysing complex internal flows and validating design concepts against experimental data[7, 8, 16]. More recently, the field had incorporated advanced computational techniques like Artificial Neural Networks (ANN) for multi-parameter performance prediction and optimization, demonstrating the potential for orders-of-magnitude increases in power output[20] . Beyond technical performance, the research scope had expanded to include sustainability analysis and hybrid systems (HSCPPs). Energy analyses assess the environmental loading of SCPPs, while hybrid configurations that co-produce electricity and green hydrogen or integrate with agriculture are being explored to improve overall economics and resource utilization[18, 21-23].

Despite these substantial advancements, critical research gaps persisted that limit commercial deployment. A primary shortcoming was the compartmentalized nature of existing research, which often investigates collector optimization, chimney design, and turbine performance in isolation[2, 6-9, 13, 14]. There is a notable lack of comprehensive studies that investigate the synergistic effects of integrating a modified collector with a purpose-designed radial turbine. Understanding how optimized collector geometries influence the inflow conditions for the turbine, and how the turbine itself must be tailored to these specific flow characteristics, remains a significant knowledge gap[3, 24]. Furthermore, while theoretical and CFD studies propose various optimizations, experimental validation of these integrated systems remains scarce. Optimizing the radial turbine's geometry was confirmed to greatly enhance the plant's power generation by improving energy extraction. Concurrently, integrating thermal storage and scaling up the system's key dimensions robustly strengthened the core buoyancy-driven airflow. Together, these approaches—refining the component and enhancing the system architecture—demonstrate complementary pathways to advance the technology's overall performance[25, 26].

Recent investigations on solar chimney power plants (SCPPs) had systematically explored multi-parameter geometric optimization[27], structural airflow enhancements[28], and comparative performance with energy towers[29]. Hananel et al. identified that a divergent chimney with a collector-to-chimney area ratio of 6 maximizes power (approximately 15 kW) using CFD and RNG k-ε modelling, while Mokrani et al. experimentally demonstrated that reducing the collector opening height and incorporating a curved junction significantly improves velocity (up to 7.2 m/s). Dalvand et al. further showed that square collectors increase airflow by 245% and that energy towers offer nocturnal operation with a threefold faster response, yet all studies collectively emphasize the critical need for transient experimental validation beyond steady-state assumptions.

The main novelties can be summarized as follows:

- Unlike conventional flat-plate collectors, our study introduces strategically placed internal guides within the collector. This modification enhances convective heat transfer, accelerates airflow, and directly addresses the low efficiency of traditional solar chimney designs. The systematic evaluation of different guide numbers (3, 6, and 9) provides new insights into their impact on velocity, pressure, and temperature distributions.
- We present a scaled 1:10 model of the Manzanares prototype, adapted to the climatic conditions of Khenchela, Algeria. This localized scaling approach is novel because it links theoretical optimization with practical energy needs of agricultural areas, ensuring contextual relevance and applicability.
- While previous works often studied collector, chimney, or turbine optimization in isolation, our research integrates these aspects into a comprehensive CFD simulation framework. This allows us to capture the synergistic effects of collector modifications on overall system performance.
- The study shows that the optimal configuration with nine guides yields a significant improvement in airflow and power output, reaching 72 W of electrical power. This quantitative evidence highlights the practical potential of our design innovation.
- We propose that further optimization of guide shapes (e.g., blade-like or inclined geometries) and coupling with turbine design could unlock additional efficiency gains. This forward-looking perspective positions our work as a foundation for next-generation solar chimney systems.

2. Modelling Of the Solar Chimney Power Plant

The solar chimney power plant (SCPP) is a sustainable system that transforms sunlight into electricity through a three-part setup: a transparent collector that traps radiation to heat the underlying air, a tall vertical stack that drives a continuous upward draft via buoyancy, and a turbine–generator unit at the chimney's base that converts the moving air's kinetic energy into mechanical then electrical power. Chimney dimensions—especially height and diameter—directly govern airflow velocity and overall efficiency, while the cycle continually exhausts cooled air to the atmosphere. To overcome the inherently low thermal capture of conventional flat collectors, this study specifically investigates the strategic placement of guides within the collector, which are designed to accelerate airflow, improve internal convective heat exchange, and boost thermal removal, thereby enhancing the plant's performance. Figure (1) and the listed dimensional specifications in table 1 detail the proposed configuration.

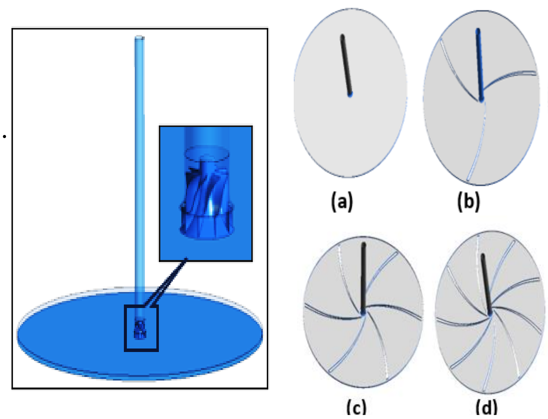

Figure 1. Different considered cases: **(a)** simple case; **(b)** with 3 guides; **(c)**; with 6 guides and **(d)** with 9 guides

Table 1. Main dimensions of the solar chimney models and of the collector guide vane

Geometric parameter	Dimensions (m)
Collector diameter (D_{col})	24.4
Collector outlet (H_1)	0.33
Chimney diameter (D_{ch})	1
Chimney height (H_{ch})	19
Guide vane span (height)	0.338
Pressure-side arc length	11.993
Suction-side arc length	11.951
Leading-edge thickness	0.400
Trailing-edge thickness	≈ 0
Thickness distribution	Monotonic taper

3.Numerical Model

3.1. Modelling assumptions

The numerical model is based on the finite volume method (FVM) to solve the governing Navier–Stokes and energy equations. The computational domain is discretized into control volumes, where the conservation equations of mass, momentum, and energy are integrated and converted into algebraic equations using the prescribed boundary conditions [6]. Owing to its robustness and accuracy, FVM is widely used for coupled fluid flow and heat transfer analyses and effectively captures the aerodynamic and thermal behavior of SCPP systems [24, 30].

The model assumes steady-state flow and heat transfer, with buoyancy effects represented by the Boussinesq approximation. Air properties are considered constant throughout the domain. Heat losses from the collector occur only through convection and radiation, while conductive losses through the collector cover are neglected. Additionally, the ambient temperature is assumed equal to the air temperature at the collector inlet for the application of the thermal boundary conditions.

3.2 Governing equations

3..2.1. The continuity equation

The equation for conservation of mass is represented by the form[31] :

$$\frac{\partial}{\partial t}\rho + \frac{1}{r}\frac{\partial}{\partial r}(r\rho u) + \frac{\partial}{\partial z}(\rho v) = 0 \tag{1}$$

3.2.2. The momentum equations

The equation of variation of momentum is shown as follows[31] :

$$\frac{\partial}{\partial t}(\rho u) + \frac{1}{r}\frac{\partial}{\partial r}(r\rho uu) + \frac{\partial}{\partial z}(\rho uv) = -\frac{\partial P}{\partial r} + \mu\left[\frac{1}{r}\frac{\partial}{\partial r}(r\frac{\partial u}{\partial r}) - \frac{u}{r^2} + \frac{\partial^2 u}{\partial z^2}\right] \tag{2}$$

$$\frac{\partial}{\partial t}(\rho v) + \frac{1}{r}\frac{\partial}{\partial r}(r\rho uv) + \frac{\partial}{\partial z}(\rho vv) = -\frac{\partial P}{\partial z} + \mu\left[\frac{1}{r}\frac{\partial}{\partial r}(r\frac{\partial v}{\partial r}) - \frac{v}{r^2} + \frac{\partial^2 v}{\partial z^2}\right] -(\rho_0 - \rho)g_z \tag{3}$$

3.2.3. Energy equation

The energy equation actually represents the mathematical text of the first law of thermodynamics and the following form will be adopted [31].

$$\frac{\partial}{\partial t}(\rho T) + \frac{\partial}{\partial r}(\rho rvT) + \frac{\partial}{\partial z}(\rho uT) = \frac{\lambda}{c_p}\left[\frac{1}{r}\frac{\partial}{\partial r}(r\frac{\partial T}{\partial r}) + \frac{\partial^2 T}{\partial z^2}\right] \tag{4}$$

3.2.4. k-ε equations

Equation of turbulent kinetic energy, k

$$\frac{\partial}{\partial t}(\rho K) + \frac{\partial}{\partial r}(\rho k\vec{V}) = div(\frac{\mu_t}{\sigma_k}\nabla k) + G_k + G_b - \rho\varepsilon \tag{5}$$

Equation of TKE dissipation rate, ε

$$\frac{\partial}{\partial t}(\rho\varepsilon) + \frac{\partial}{\partial r}(\rho\varepsilon\vec{V}) = div(\frac{\mu_t}{\sigma_\varepsilon}\nabla\varepsilon) + C_{1\varepsilon}(G_k + G_b) - \frac{C_{2\varepsilon}\rho\varepsilon}{k} \tag{6}$$

Where μ_t is the turbulent viscosity, given as:

$$\mu_t = \rho C_\mu \frac{k^2}{\varepsilon} \tag{7}$$

The generation of turbulent kinetic energy G_k and the buoyancy production term G_b are given as follows:

$$G_k = R_{ij}\frac{\partial u_i}{\partial x_j} \tag{8}$$

$$G_b = \beta\frac{g}{T}\mu_t\frac{\partial T}{\partial y} \tag{9}$$

The five empirical constants of *k*-*ε* model are typically set as in table 2

Table 2. Constants of k-ε turbulence model

$C_{1\varepsilon}$	$C_{2\varepsilon}$	C_μ	σ_k	σ_ε
1,44	1,92	0,09	1	1,3

3.2.5. The power and the thermal efficiency

Thermal efficiency is the primary performance metric used to compare distinct designs for any work. For the solar chimney, it is calculated using the following equation[7]:

$$\eta_{tot} = \frac{\frac{1}{2}\rho A_{ch} V_{ch}^3}{I A_{co}} \qquad (10)$$

ρ: Density of air (kg/m^3). A_{ch}: The cross-sectional area of the chimney at the base (m^2). V_{ch}: Air velocity at the base of the chimney (m/s). I: Solar radiation (W/m^2). A_{co}: Solar collector area (m^2).

Based on the most published works the accessible power yield P of the SCPP is calculated from the following equation[32]:

$$P = \eta_{tot} A_{co} I \qquad (11)$$

4. Solution settings

The steady-state Reynolds-Averaged Navier–Stokes (RANS) equations were solved using the commercial CFD code ANSYS Fluent. The pressure–velocity coupling was handled via the SIMPLE algorithm, with the RNG scheme employed for pressure discretization and the 'Second Order Upwind' scheme applied to the momentum, turbulent kinetic energy, and dissipation rate equations. To ensure rigorous numerical and physical stability, a multi-tiered convergence criteria was established. Specifically, the scaled residuals for continuity and momentum were required to drop below 1×10^{-4}, while the turbulence quantities (k and ε) were permitted to plateau below 1×10^{-5} due to their inherent numerical stiffness. Crucially, convergence was not solely judged by residuals; the total pressure rise across the guide vane domain was monitored as a primary physical control variable. The simulation was deemed fully converged only when this monitored pressure maintained a stable variation of less than 0.2% over the final 200 iterations, confirming that the macroscopic flow field had reached a steady state. Additionally, the global mass imbalance between the inlet and outlet was strictly maintained below 0.1% to guarantee overall conservation of mass.

5. Boundary Conditions

The computational domain frontiers identification is shown in figure (2) and affecting boundary conditions that were used in each simulation are displayed in table 3.

The dynamic boundaries describe that the system inlet represents the ambient conditions with respect to temperature T_0 and atmospheric pressure, while we adopted a pressure estimated at P = 0 Pas for the outlet. The mixed model solves the heat transfer through convection and radiation modes. The radiation incident on the collector is integrated by the DO model. The collector wall is considered semi-transparent. As for the chimney wall, we consider it adiabatic due to neglecting the heat change resulting from the insulation of the chimney wall. For the input metrological data, the solar radiation and the ambient temperature are given by the values measured on June 21th at 13 h.

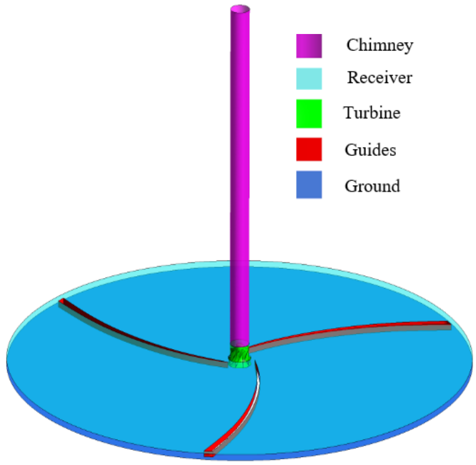

Figure 2. Boundary conditions

Table 3. Boundary conditions used in simulation

Location	Type	Parameters
Collector roof	Semi-transparent wall	DO radiation; h=10 W/m². K ; T_0=313K ; T_{sky}=0.0552 $T_0^{1.5}$
Ground	Wall	Q=0 (adiabatic)
Chimney	Wall	Q=0
Inlet	Pressure inlet	P=0 Pa ; T_0=313k
Outlet	Pressure outlet	P= 0 Pa

For the solid domains, Table 4 provides Ground, Steel and collector's densities, specific heats, and thermal conductivities. First, the steel's thermal diffusivity is the highest among the three materials, which explains its ability to conduct the maximum heat from the absorber plate. Second, the thermal conductivity of the collector material is the lowest of all, making it a good choice for insulation and limiting heat loss to the bottom surface.

Table 4. physical properties of the materials used in the CFD simulation

Property	Air	Ground	Steel	Collector
Density ($kg.m^{-3}$)	1.225	1900	8030	2700
Specific heat capacity ($J.kg^{-1}.k^{-1}$)	1006.43	2200	502.48	840
Thermal conductivity ($W.m^{-1}.k^{-1}$)	0.0242	1.83	16.27	0.78
Thermal expansion coefficient	0.0033	___	___	___

For the fluid domain, density, specific heat, thermal conductivity, and the volumetric thermal expansion coefficient were set to 1.225 kg/m^3, 1006.43 J/kg.K, 0.0242 W/m.K and 0.0033 K^{-1}, respectively. It is especially important to note the thermal expansion coefficient and its contribution to the natural convection in the collector cavity's fluid domains.

The thermal expansion coefficients for solid materials were not included because they do not impact the flow field at the operating temperature range and have no effect on the convection solution in the conjugate heat transfer model.

The properties mentioned above play a significant ro le in determining conduction and convection heat transfer mechanisms at fluid-solid interfaces.

Validating the grid independence examination is a crucial step in CFD. It allows for incorporating the optimal compromise among computational time and simulation accuracy. In this study the evaluation of maximum velocity was approved by performing the simulation for one of the four cases studied. The analytic comparison of the number of elements and nodes leads to identify the appropriate element size, ensuring both the reliability of results and numerical efficiency. Three mesh configurations different mesh densities, 309688 elements, 139138 elements, 93205 elements, were examined (table 5). The quality of each mesh was evaluated using skewness and orthogonality, The majority of mesh elements exhibit skewness values below 0.25, indicating excellent to very good mesh quality. For orthogonal quality, values from 0.89–0.98 indicate excellent quality, which supports the accuracy and reliability of the CFD results, especially in the narrow regions.

Table 5. Grid independence details result for the CFD model

Number of nodes	Number of elements	V_{max} (m/s)
291492	309688	4.37
122512	139138	4.30
74484	93205	4.41

5.1 Turbulence model sensitivity

The predictions for the examined solar chimney flow are largely insensitive to the turbulence model selection. Despite the known advantages of the k-ω SST model for separated and boundary-layer flows, the standard k-ε model achieves comparable accuracy here. Consequently, the k-ε model is selected for its lower computational expense (Fig. 3).

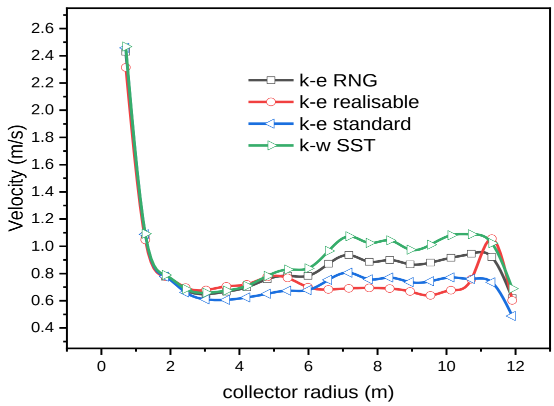

Figure 3. Velocity distribution thorough collector for the different turbulence models; case zero guides.

Table 6. Overview of key simulation parameters considered in present study and literature data

Ref	Collector Diameter (M)	Chimney Diameter(M)	Chimney Height (M)	V max (m/s)	T max (ΔT)
Our study	24.4	1	19	5.16	11.4
Maia et al. 2017	25	1	12.3	2.21±0.132	26.5±1.1
Buğutekin 2010	27	0.8	17.15	5	25
Maia et al. 2009	25	1	11	2.5±0.165	30±1.4
Ferreira et al.2008	25	1	12.3	2.75±0.165	27±0.5

To validate our numerical model, we compared our geometric inputs and performance outputs against established literature, as shown in Table 6. Our collector diameter (24.4 m) and chimney diameter (1.0 m) closely match most reference studies (Maia et al., 2009, 2017; Ferreira et al., 2008). However, our chimney height (19 m) is significantly taller than the 11–12.3 m range reported in most studies, though comparable to Buğutekin (2010) at 17.15 m.
This taller chimney enhances the buoyancy-driven draft, yielding a maximum air velocity of 5.16 m/s—substantially higher than the 2.21–2.75 m/s reported by Maia and Ferreira, but in close agreement with Buğutekin's 5 m/s benchmark. However, this increased velocity comes at a thermal cost: the accelerated airflow reduces residence time over the absorber, producing a maximum temperature difference (ΔT) of only 11.4 °C, significantly lower than the 26.5–30 °C range found in the literature.
This inverse relationship between velocity and temperature confirms the classical trade-off between flow rate and thermal absorption, demonstrating that our model behaves physically. These results validate the reliability of our computational approach, giving us confidence to use this model for further investigations into obstacle placement within the collector.

6.Validation

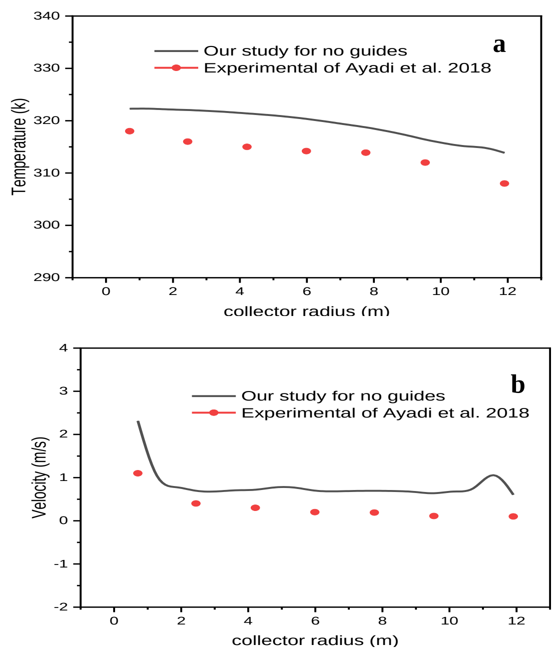

Figure 4. Numerical vs. experimental.
(a) Temperature and **(b)** air velocity through the collector

In this study, the numerical results were juxtaposed against the experimental by Ayadi et al [33]for qualitative corroboration. The lack of a sufficient quantitative metric for a point-wise error assessment leads to the comparison thus being very phenomenological. However, the numerical predictions produce a fantastic agreement with the reference data (figure 4) , exactly reproducing the same asymptotic saturation behavior and similar curvature observed along the entire transient regime. This qualitative agreement supports the capability of the model to reproduce the primary mechanisms driving this behavior.

7.Results and Discussion

To investigate the effect of the presence of guides within the collector on velocity, static pressure and static temperature distribution, a series of designs incorporating a fixed number of guides were analysed.
For the configuration with 9 guides, Figure (5) shows a velocity range of 0 to 3.04 m/s. The results indicate a low velocity at the collector inlet, with the highest values occurring at the chimney base. The velocity profile remained consistent from the base to the chimney exit. Also, the pressure field demonstrates an inverse relationship to velocity figure (6); reaching its minimum at the base of chimney ranging from 0pa to -0.41 pa. The temperature distribution, shown in Figure (6), varied within the collector, ranging from 313 K to 322.9 K.
For case (c), a similar trend was observed. The velocity ranged from 0 to 2.8 m/s (Figure 5), again peaking at the chimney base. For the pressure value decrease from 0 to -0.22 pa figure (6); The temperature range was slightly lower, between 313 K and 322.6 K, while still demonstrating clear variation across the collector Figure (4).
A comparative analysis of cases (a) and (b) is presented in Figures 5 and 6. The maximum velocities were 2.3 m/s and 2.6 m/s for cases (a) and (b), respectively. And minimum values of pressure of -0.15pa and 0.03 pa. Correspondingly, the maximum temperatures reached 322.3 K for case (a) and 322.7 K for case (b) (Figure 7). These results confirm that temperature variation inside the collector is a consistent feature across all configurations tested.
About the streamlines which shown in figure (8) the velocity through the collector gradually increased due to the existence of guides, the maximum velocity achieved at 3 m/s for the case (d), as well the high temperature due to accelerate the flow within the collector; as observed the velocity in chimney decelerate due to wall shear.

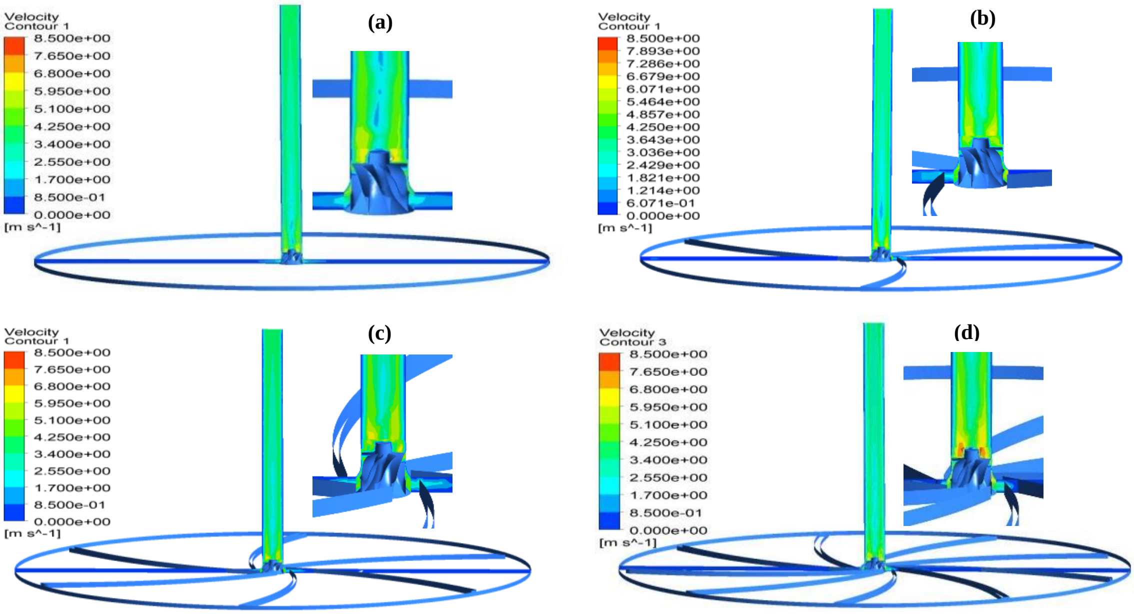

Figure 5. Distribution of velocity for the four considered cases: (a) ; (b); (c) and (d)

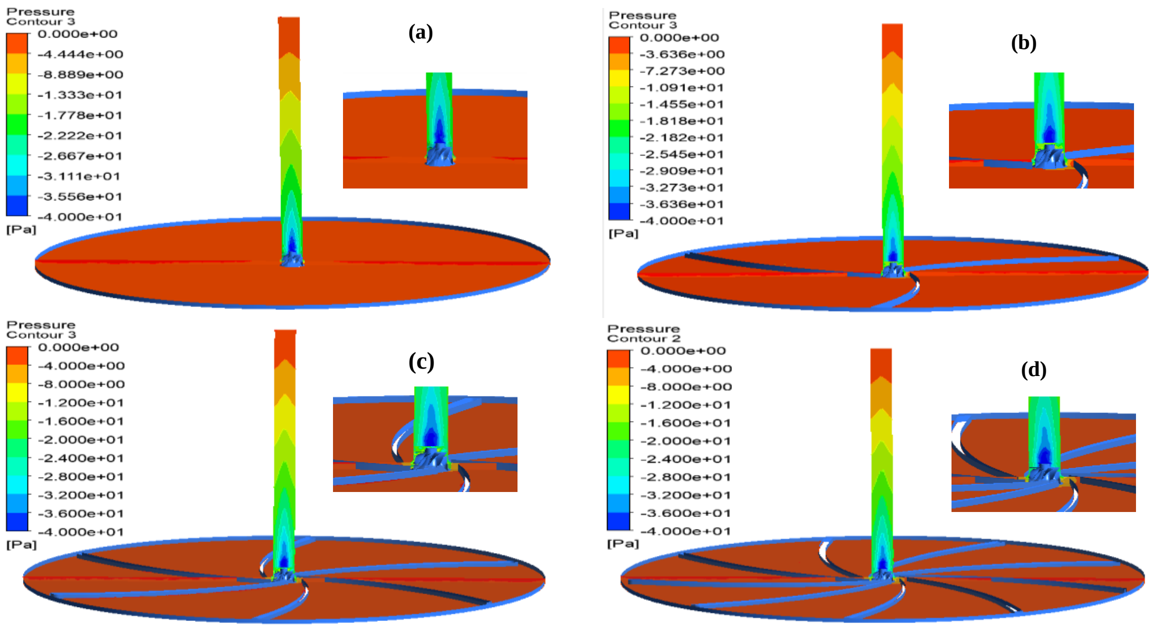

Figure 6. Distribution of pressure for the four considered cases: (a); (b); (c) and (d)

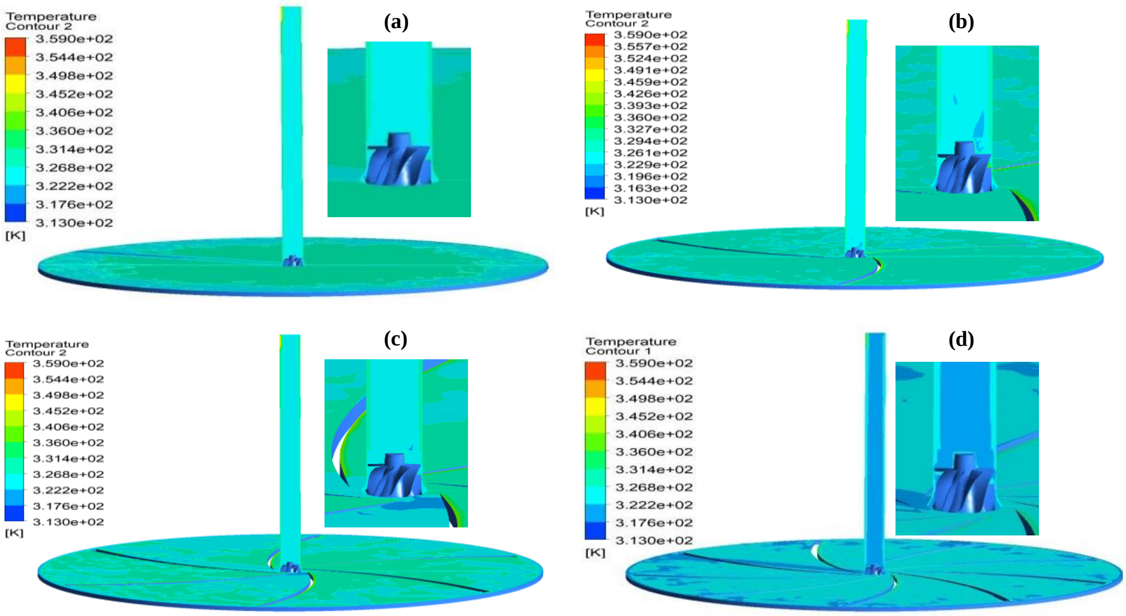

Figure 7. Distribution of temperature for the four considered cases : (a) ; (b); (c) and (d)

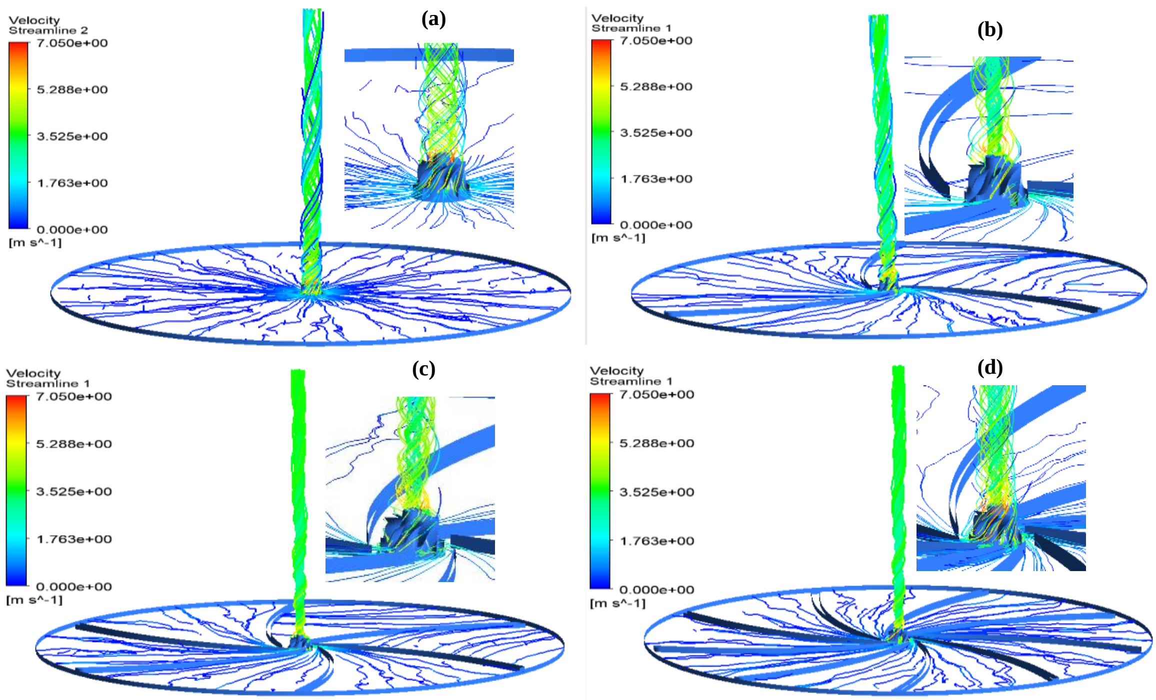

Figure 8. Streamlines for the four considered cases: (a); (b); (c) and (d)

7.1. Collector results

Analysis of the results and corresponding graphs (Figures 9 ,10and 11) reveals distinct trends in airflow behaviour.

The air velocity (figure 9), initially at a minimum of 0.7 m/s at the collector inlet, exhibits different progression patterns depending on the configuration. In Cases (a), (b), and (c), the velocity remains relatively constant between 0.7 m/s and 1.04; 1.34; 1.41 m/s until approximately two meters from the collector outlet, where a sharp increase occurs, peaking at the chimney base with respectively values of 2.31 ;2.57; 2.83 m/s. In contrast, Case (d) shows a more gradual increase from the inlet 0.7m/s to 3.04 m/s at the collector outlet.

Unlike velocity, static pressure reaches its minimum at the outlet of collector where intense flow convergence and buoyancy effects result in a significant pressure decrease accelerating the flow (figure 10). In Cases (a), (b), and (c), pressure remains relatively constant between 0 pa and -0.33; -0.56; -0.75 pa until approximately 1.5 meters from outlet of the collector, where a sharp decrease occurs until reaches respectively values of -6.06 ; -7.12; -9.20 pa. In contrast, Case (d) shows a more gradual decrease to -9.98 pa at the collector outlet.

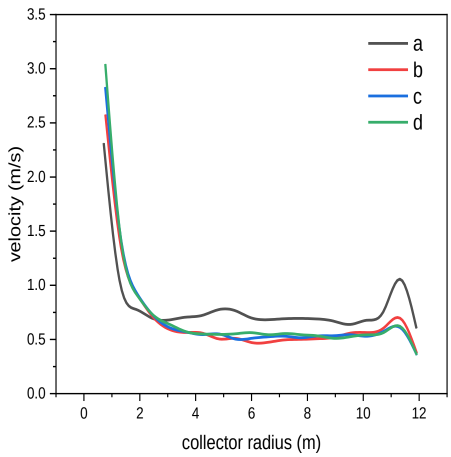

Figure 9. Average of velocity through the collector for the four considered cases: (a) ; (b); (c) and (d)

Concurrently, the air temperature demonstrates a consistent trend across all cases, increasing gradually from a minimum at the inlet (313 K) to a maximum at the collector outlet. The final outlet temperatures were 323.18 K for Case (d), 322.83 K for Case (b), 322.62 K for Case (c), and 322.29 K for Case (a) (figure 11).

In summary, while the temperature rise is consistent, the velocity profile is significantly influenced by the internal configuration of the collector. The results indicate that the presence and number of guides induce marked variations in air velocity, with Case (d) demonstrating the most pronounced acceleration. This highlights the critical role of collector design in modulating the thermodynamic properties of the airflow.

As a conclusion regarding velocity, at the collector inlet, the velocity is minimum but gradually increases as air passes through the collector, reaching its maximum at the exit. This increase is most pronounced for case (d)with 9 guides, followed by less pronounced increases for cases (a),(b) and (c).

regarding pressure, we note an inverse trend compared to pressure; there is a marked variation

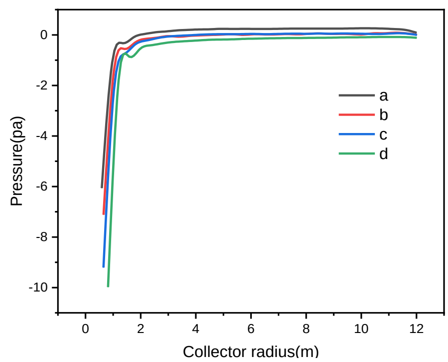

Figure 10. Average of static pressure through the collector for the four considered cases : (a) ; (b); (c) and (d)

along the airflow path in the collector. At the inlet, the pressure reaches its maximum but decreases rapidly as air moves through the collector toward the outlet. Again, this reduction is particularly noticeable for case (d), followed by a slightly less pronounced (a), (b) and (c).

As for the air temperature, it also changes along the way to the exit. We observe a gradual increase in temperature, with a minimum temperature at the inlet and a maximum temperature at the collector outlet. This increase is more significant for case (d) and slightly attenuated for (a),(b) and (c). In summary, these observations highlight the importance of the guided collector on the parameters studied. A number of guides appear to induce less marked variations in the distribution of pressure, velocity, and temperature of the air inside the collector. The case of 9 guides shows distinct behaviour compared to other cases, with notable differences in pressure, velocity, and temperature changes.

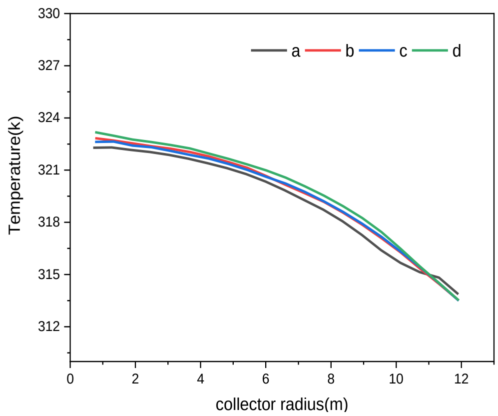

Figure 11. Average of static temperature through the collector for the four considered cases : (a) ; (b); (c) and (d)

7.2. Chimney results

For the chimney (figure (12-14)), we observed phenomena quite different from those of the collector:
7.2.1. Air velocity: regarding the velocity, A notable surge in velocity consistently occurs at the base of the chimney in the first 2 meters, offering valuable insights into the rate of rotation of the turbine then we note a sudden drop from 4.97 m/s to 3.60 m/s for the case a; for b and c the drop is from 4.86 m/s ; 4.93 m/s to 3.63 m/s;3.65 m/s respectively; while the case d the decrease is from 5.12 m/s to 3.55 m/s, followed by a stabilization until the exit from the chimney.
7.2.2. Pressure: observations vary depending on the existing of guides within the collector. At all cases pressure increases as air moves toward the chimney exit. For case (d), the pressure values between -29.57 pa to 0 pa at the exit of chimney, for the other cases (a), (b)and (c) it decreases from -28.07 ,-22.75 , -24.17 pa respectively to reaches the atmospheric pressure at the outlet. However, the graph shows a similar trend for all four cases.
7.2.3. Air temperature: we observe subtle but distinct variations. For cases (b) and (d) an almost match observed for both curves, the temperature decreases from 324.16 k , 324.18 k to 323.07 k. On the other hand, for cases (c) and (a), the temperature experiences drop from 324.02 k ,323.66 k to 322.92 k ,322.61 k respectively at the outlet of the chimney, as indicated in the values provided (drop in temperature within chimney until the flow exits up).

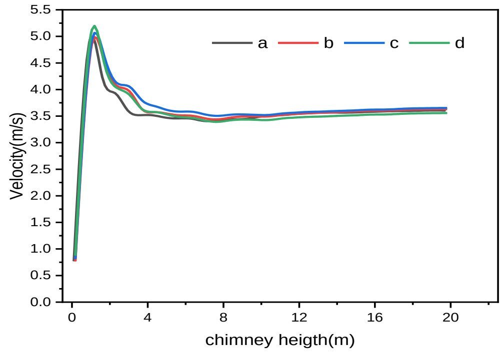

Figure12. Average n of velocity through the chimney for the four considered cases : (a) ;

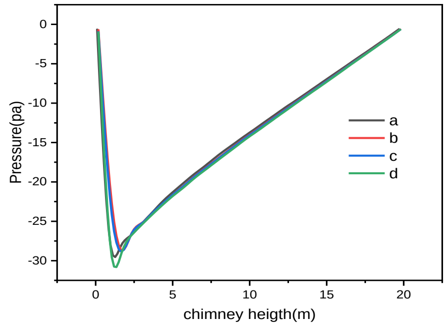

Figure 13. Average of static pressure through the chimney for the four considered cases : (a) ; (b); (c) and (d)

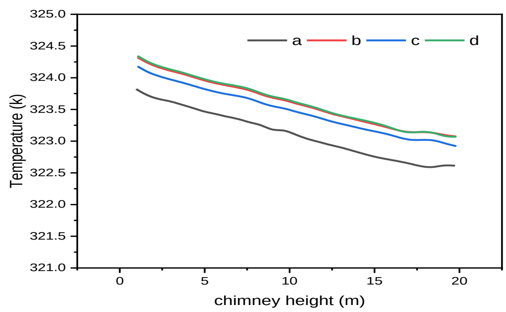

Figure 14. Average of static temperature through the chimney for the four considered cases : (a) ; (b); (c) and (d)

Figure (15,16) represents average of velocity and static temperature through the chimney and the collector respectively for different solar irradiation varied from 600 to 1600 w/m^2 for the optimum case (d) with 9 guides; it is remarked the direct proportion between the temperature and the solar radiation (figure 17).

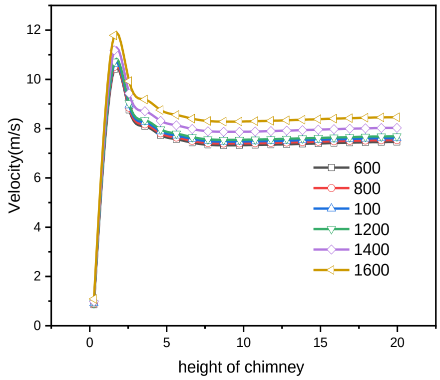

Figure15. Average of velocity through the chimney for different solar radiation for the case (d)

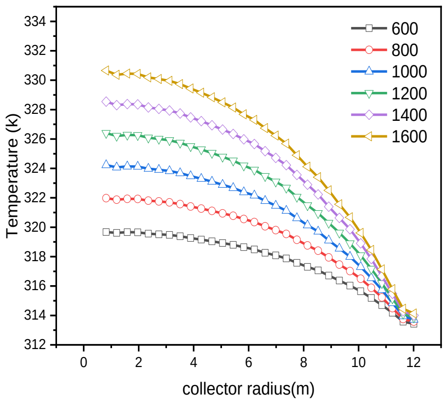

Figure16. Average of static temperature through the collector for different solar radiation for the case (d)

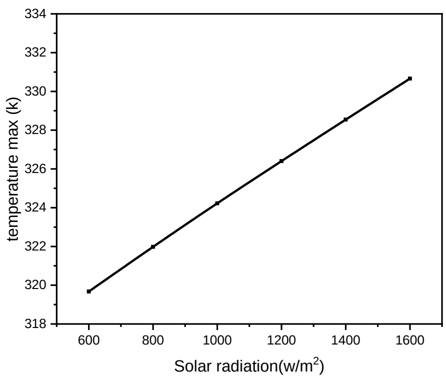

Figure 17. Maximum static temperature for different solar irradiation for the case (d)

Figure (18) represents the power output as a function of the different studied cases of the collector; from this outcome we observe that for case (d) we obtained the higher value of energy with value of 72 Watts, the case (a) gave the lower value which is equal to 56 watts. From this place we deduce that the presence of the guides within the collector affects the power output.

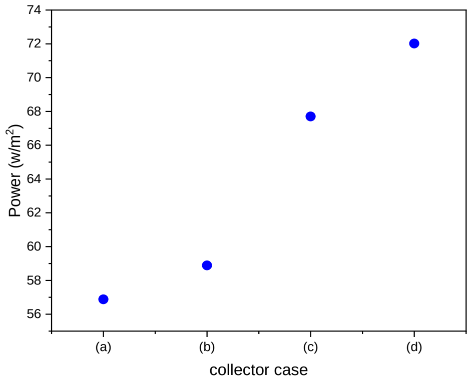

Figure 18. power output for the four considered cases : (a) ; (b); (c) and (d)

8. Conclusions

This study numerically investigated the influence of integrating internal flow guides within the collector of a solar chimney power plant (SCPP) using a three-dimensional CFD model based on a 1:10 scaled Manzanares prototype adapted to the climatic conditions of Khenchela, Algeria. Unlike conventional SCPP configurations, the proposed design introduces passive flow-guiding elements to modify the airflow structure inside the collector, with the objective of improving the overall aerodynamic and thermal performance of the system.

A systematic parametric analysis was carried out for collector configurations with 3, 6, and 9 internal guides, and their performances were compared with the conventional collector without guides. The numerical results demonstrate that increasing the number of guides enhances the airflow characteristics by improving pressure distribution and maintaining a more favorable thermal field while promoting a more stable airflow toward the chimney. Among the investigated configurations, the collector equipped with nine guides (Case d) exhibited the best overall performance.

The optimal configuration generated the highest chimney inlet pressure, maintained a more uniform temperature distribution along the flow path, and produced the greatest electrical power output of approximately 72 W, demonstrating the effectiveness

of the proposed passive flow-control strategy. These results confirm that properly designed internal guides can significantly improve the aerodynamic behavior of the collector and consequently enhance the energy conversion capability of the solar chimney system.
The principal contribution of this work is the demonstration that collector-integrated internal flow guides constitute an effective passive design approach for improving SCPP performance. In addition, the study provides a comprehensive CFD framework for evaluating the coupled effects of collector modifications on the thermal and fluid dynamic behavior of the entire system, offering useful design guidelines for future solar chimney developments under site-specific climatic conditions. Future work will focus on optimizing the guide geometry by investigating blade-shaped, curved, and inclined guide configurations to further enhance airflow acceleration and heat transfer. In addition, coupling the optimized collector with a dedicated turbine design and performing multi-objective optimization of both components are expected to further improve the overall efficiency and power output of solar chimney power plants.

Nomenclature

A_{ch}	The cross-sectional area of the chimney at the base (m^2)
A_{co}	Solar collector area (m^2)
$C_{1\varepsilon}$, $C2\varepsilon$,	Empirical constants of k–ε model
C_p	Heat capacity (kJ/K)
D_{col}	Collector diameter (m)
D_{ch}	Chimney diameter (m)
Gb	Buoyancy production term (m^2s^{-2})
Gk	Turbulent kinetic energy (m^2s^{-2})
g	Gravitational acceleration (m/s^2)
H_1	Output collector (m)
H_2	Input collector (m)
H_{ch}	Chimney height (m)
I	Solar radiation (W/m^2)
K	Turbulent kinetic energy(m^2s^{-2})
p	Pressure (Pa)
P	Power (watts)
R_{ij}	Reynolds stress tensor
R	Radial coordinate
T	Temperature (k)
V_{ch}	Air velocity at the base of the chimney (m/s)
v	Absolute velocity(m/s)
Vr	Relative velocity (m/s)
β	Coefficient of thermal expansion (k^{-1})
ε	Rate of dissipation of turbulent energy(m^2s^{-3})
μt	The turbulent viscosity
η tot	Total efficiency of SCPP
λ	Thermal conductivity
ρ0	Reference density(kg/m^3)
ρ	Density of the air (kg/m^3)
IFR turbine	Inflow radial turbine
CFD	Computational fluid dynamics
FVM	Finite volume method
MRF	multiple reference frame

References

1. Ming, T., et al., *Chimney shape numerical study for solar chimney power generating systems.* International Journal of Energy Research, 2013. **37**(4): p. 310-322. https://doi.org/10.1002/er.1910
2. Tingzhen, M., et al., *Numerical simulation of the solar chimney power plant systems coupled with turbine.* Renewable Energy, 2008. **33**(5): p. 897-905. https://doi.org/10.1016/j.renene.2007.06.021
3. Biswas, N., et al., *Experimental Treatment of Solar Chimney Power Plant—A Comprehensive Review.* Energies, 2023. **16**(17). https://doi.org/10.3390/en16176134
4. Zhu, L., et al., *A comprehensive review of solar chimney power plants: technology, performance, and future prospects.* Sustainable Energy Technologies and Assessments, 2025. **81**: p. 104413. https://doi.org/10.1016/j.seta.2025.104413
5. Das, P. and C. Vp, *A critical review on solar chimney power plant technology: influence of environment and geometrical parameters, barriers for commercialization, opportunities, and carbon emission mitigation.* Environmental Science and Pollution Research, 2022. **29**. https://doi.org/10.1007/s11356-022-22623-7

6. Keshari, S., C. Vp, and P. Das, *A 3D numerical study to evaluate optimum collector inclination angle of Manzanares solar updraft tower power plant.* Solar Energy, 2021. **226**: p. 455-467. https://doi.org/10.1016/j.solener.2021.08.062
7. Gholamalizadeh, E. and M.-H. Kim, *CFD (computational fluid dynamics) analysis of a solar-chimney power plant with inclined collector roof.* Energy, 2016. **107**: p. 661-667. https://doi.org/10.1016/j.energy.2016.04.077
8. Das, P. and C. Vp, *Effect of chimney height and collector roof angle on flow parameters of solar updraft tower (SUT) plant A 3D numerical analysis.* Journal of Thermal Analysis and Calorimetry, 2018. **136**: p. 133-145. https://doi.org/10.1007/s10973-018-7749-y
9. Aziz, M. and A. Elsayed, *Thermofluid effects of solar chimney geometry on performance parameters.* Renewable Energy, 2022. **200**. https://doi.org/10.1016/j.renene.2022.10.022
10. Okada, S., et al., *Improvement in Solar Chimney Power Generation by Using a Diffuser Tower.* Journal of Solar Energy Engineering, 2015. **137**: p. 031009. https://doi.org/10.1115/1.4029377
11. Mandal, D., et al., *Impact of chimney divergence and sloped absorber on energy efficacy of a solar chimney power plant (SCPP).* Ain Shams Engineering Journal, 2023. **15**: p. 102390. https://doi.org/10.1016/j.asej.2023.102390
12. Cuce, E., et al., *Performance assessment of solar chimney power plants with natural thermal energy storage materials on ground: CFD analysis with experimental validation.* International Journal of Low-Carbon Technologies, 2022. **17**: p. 752-759. https://doi.org/10.1093/ijlct/ctac001
13. Kasaeian, A., et al., *3D simulation of solar chimney power plant considering turbine blades.* Energy Conversion and Management, 2017. **147**: p. 55-65. https://doi.org/10.1016/j.enconman.2017.05.029
14. Caicedo, P., D. Wood, and C. Johansen, *Radial Turbine Design for Solar Chimney Power Plants.* Energies, 2021. **14**(3). https://doi.org/10.3390/en14030674
15. Alshammari, F., N. ben khedher, and L. Ben Said, *Development of an Automated Design and off-design Radial Turbine Model for Solar Organic Rankine Cycle Coupled to a Parabolic Trough Solar Collector.* Applied Thermal Engineering, 2023. **230**: p. 120677. https://doi.org/10.1016/j.applthermaleng.2023.120677
16. Azizi, A., et al., *Experimental and CFD investigation of small-scale solar chimney for power generation. Case study: southeast of Algeria.* Desalination and Water Treatment, 2019. **160**: p. 1-8. https://doi.org/10.5004/dwt.2019.24167
17. Maghrebi, M.J., R. Masoudi Nejad, and S. Masoudi, *Performance analysis of sloped solar chimney power plants in the southwestern region of Iran.* International Journal of Ambient Energy, 2016. **38**(6): p. 542-549. https://doi.org/10.5004/dwt.2019.24167
18. Marzouk, O.A., *Energy Generation Intensity (EGI) of Solar Updraft Tower (SUT) Power Plants Relative to CSP Plants and PV Power Plants Using the New Energy Simulator "Aladdin".* Energies, 2024. **17**(2). https://doi.org/10.3390/en17020405
19. Smaisim, G.F., et al., *Modeling the Thermal Performance for Different Types of Solar Chimney Power Plants.* Complexity, 2022. **2022**(1). https://doi.org/10.1155/2022/3656482
20. Mandal, D.K., et al., *An application of artificial neural network (ANN) for comparative performance assessment of solar chimney (SC) plant for green energy production.* Sci Rep, 2024. **14**(1): p. 979. https://doi.org/10.1038/s41598-023-46505-1
21. Elsayed, I. and Y. Nishi, *Emergy and Sustainability Ternary Diagrams of Energy Systems: Application to Solar Updraft Tower.* Sustainability, 2020. **12**(24). https://doi.org/10.3390/su122410546
22. Jemal, A., et al., *Optimization of hybrid solar chimney power plant using Pearson and k-means analysis for green hydrogen and electricity production.* Scientific Reports, 2025. **15**.

https://doi.org/10.1038/s41598-025-24507-5

23. Mandal, D.K., et al., *Optimization of hybrid solar chimney power plants (HSCPPs): A review of multi-objective approaches*. Applied Energy, 2025. **396**. https://doi.org/10.1016/j.apenergy.2025.126214

24. Bourgouin, J.-F., et al., *Sensitivity of swirling flows to small changes in the swirler geometry*. Comptes Rendus. Mécanique, 2013. **341**(1-2): p. 211-219. https://doi.org/10.1016/j.crme.2012.10.018

25. Bouzida, Y., et al., *Computational Analysis of Radial Turbine Design and Performance for Renewable Power Generation in Solar Chimney*. Journal of Solar Energy Research, 2025. **10**(4): p. 2603-2615. https://doi.org/10.22059/jser.2025.404342.1658

26. Yagnik, B. and B. Ramani, *A Computational Study on The Effect of Geometrical Configurations on Axisymmetric Solar Chimney Performance*. Journal of Solar Energy Research, 2025. **10**(4): p. 2645-2656. https://doi.org/10.22059/jser.2025.404298.1652

27. Hananel, A., R. Garcia, and A. Vera, *Optimization of solar chimney performance through CFD modelling and parametric experimental design*. An International Journal of Optimization and Control: Theories & Applications (IJOCTA), 2026. **16**(2). https://doi.org/10.36922/IJOCTA025430181

28. Mokrani, O.B.E., et al., *Enhancing thermo-aerodynamic performance of solar chimney power plants*. Journal of Thermal Analysis and Calorimetry, 2026. **151**(3): p. 2567-2585. https://doi.org/10.1007/s10973-025-15258-6

29. Dalvand, M., R. Mehdipour, and Z. Baniamerian, *Experimental comparison of solar chimney and energy tower systems for clean power generation*. Journal of Thermal Analysis and Calorimetry, 2026. **151**(7): p. 6329-6342. https://doi.org/10.1007/s10973-026-15424-4

30. Patankar, S., *Numerical heat transfer and fluid flow*. 2018. https://doi.org/10.1201/9781482234213

31. Ayadi, A., Z. Driss, and M.S. Abid, *Experimental and computational analysis of the collector geometry of a solar chimney*. Environmental Progress & Sustainable Energy, 2019. **38**(6). https://doi.org/10.1002/ep.13238

32. Ayadi, A., et al., *A computational and an experimental study on the effect of the chimney height on the thermal characteristics of a solar chimney power plant*. Proceedings of the Institution of Mechanical Engineers, Part E: Journal of Process Mechanical Engineering, 2017. **232**(4): p. 503-516. https://doi.org/10.1177/0954408917719776

33. Ayadi, A., et al., *Effect of the turbine diameter on the generated power of a solar chimney power plant*. Energy & Environment, 2018. **29**(5): p. 822-836. https://doi.org/10.1177/0958305x18761148